Petroleum Science 23 (2026) 475–485

Contents lists available at ScienceDirect

Petroleum Science

journal homepage: www.keaipublishing.com/en/journals/petroleum-science

Original Paper

Insight into the impact of the Al distribution in ZSM-5 zeolite on deep hydrogenation of phenanthrene over Pt/HZSM-5

Chuan-Hao Zhang [a], Qi Dong [a], Fei Wang [a], Ning-Yue Lu [b], Feng Yu [a,*], Bin-Bin Fan [a,**], Rui-Feng Li [a,***]

[a] College of Chemistry and Chemical Engineering, Taiyuan University of Technology, Taiyuan, 030024, Shanxi, China
[b] School of Pharmacy, Changzhi Medical College, Changzhi, 046000, Shanxi, China

ARTICLE INFO

Article history:
Received 4 March 2025
Received in revised form
12 June 2025
Accepted 9 September 2025
Available online 13 September 2025

Edited by Min Li

Keywords:
Zeolite
ZSM-5
Al distribution
Pt/HZSM-5
Phenanthrene
Deep hydrogenation

ABSTRACT

Deep hydrogenation of polycyclic aromatic hydrocarbons (PAHs) into jet fuel is an important strategy for the upgrading of light cycle oil (LCO). Zeolite-supported metal catalysts have exhibited good catalytic performance for hydrogenation of PAHs under relatively mild conditions. However, the impacts of acidity variations in zeolite supports, arising from the differences in framework Al (Al_F) distribution on the catalytic behavior of zeolite-supported metal catalysts in the deep hydrogenation of PAHs remains unclear. Herein, two series of mesoporous ZSM-5 samples, that is ZSM-5-E-*x* and ZSM-5-F-*x*, with the differences in Al_F distribution but similar Si/Al ratios, were prepared in the crystallization system with or without NaOH. The results of NH_3-TPD, Pyridine-IR, N_2 adsorption-desorption and SEM reveal that two series of HZSM-5 samples have similar acid density and acid strength, textural properties, morphology and particle size. However, the results of XPS, ^{27}Al MAS NMR, 2,6-Ditert-butylpyridine-IR, catalytic cracking of 1,3,5-triisopropylbenzene and the controlled reactions as well as DFT calculation indicate that the higher enrichment degree of Al_F on the external surface and the suitable arrangement mode of Al_F in ten-membered ring (10-MR) of HZSM-5-F-*x* compared to HZSM-5-E-*x* in case of the similar Si/Al ratios, result in Pt/HZSM-5-F-*x* exhibiting remarkably-improved deep hydrogenation performance of phenanthrene (PHE) compared to Pt/HZSM-5-E-*x*. Particularly, the selectivity to perhydrophenanthrene (PHP) over Pt/HZSM-5-F-50 can reach above 99.0% at a conversion of PHE (>99.0%). Furthermore, Pt/HZSM-5-F-50 exhibits well reusability. This work helps to clarify the impact of Al_F distribution in ZSM-5 on catalytic hydrogenation performance for PAHs, providing valuable guidance for design and development of efficient catalysts for the hydrogenation of PAHs.

1. Introduction

The light cycle oil (LCO), a low value-added product obtained though fluid catalytic cracking (FCC), contains abundant polycyclic aromatic hydrocarbons (PAHs, including bicyclic and tricyclic hydrocarbons, up to 90.0%), such as naphthalene, anthracene and phenanthrene (Laredo et al., 2018; Peng et al., 2019; Zhang et al., 2022; Dong et al., 2023). Deep hydrogenation of PAHs into cycloalkanes, which can be used as blending components of jet fuel range (Zhang et al., 2016, 2019b), lubricant base oil and refrigeration oil (Wang et al., 2016; Wang et al., 2019; Jia et al., 2021), is a promising high value conversion strategy. However, the deep hydrogenation of PAHs, especially tricyclic aromatic hydrocarbons such as phenanthrene or anthracene, remains a great challenge due to the increasing resonance energy and steric hindrance effects during the step-by-step hydrogenation saturation of PAHs. Thus, development of an efficient catalyst for deep hydrogenation of PAHs is highly significant.

In hydrogenation of PAHs, the hydrogenation capability of the catalysts shows a correlation with the adsorption behavior of PAHs on the catalysts, which mainly depends on the size and structure of PAHs. Generally, the adsorption capacity of the PAHs on

* Corresponding author.
** Corresponding author.
*** Corresponding author.
E-mail addresses: yufeng@tyut.edu.cn (F. Yu), fanbinbin@tyut.edu.cn (B.-B. Fan), rfli@tyut.edu.cn (R.-F. Li).

Peer review under the responsibility of China University of Petroleum (Beijing).

https://doi.org/10.1016/j.petsci.2025.09.017

catalysts increases with the number of aromatic rings, and the linear PAHs have stronger adsorption capability than the non-linear PAHs (Beltramone et al., 2008; Dang et al., 2019). Deep hydrogenation of PAHs is a tandem reaction process, involving the sequential hydrogenation of the generated various aromatic intermediates with the distinct steric hindrance. Thus, the deep hydrogenation degree of PAHs usually depends on the hydrogenation of the intermediates. For instance, the conversion of symmetric octahydrophenanthrene (sym-OHP) to perhydrophen anthrene (PHP) is the rate-determining step in deep hydrogenation of phenanthrene (PHE), primarily due to the steric hindrance in the adsorption of sym-OHP on the catalyst surface and competitive adsorption with partially hydrogenated aromatics (Jongpatiwut et al., 2004; Beltramone et al., 2008; Qi et al., 2014; Fu et al., 2015; Wang et al., 2019). Therefore, enhancing the adsorption capacity for the intermediates with the larger steric hindrance on the catalysts is an effective strategy to improve the deep hydrogenation performance of the catalysts for PAHs.

Traditionally, supported metal catalysts have been widely used in many hydrogenation reactions (Tang et al., 2008; He et al., 2013; Zhu et al., 2017; Liu and Corma, 2018; Luo et al., 2018; Liu et al., 2020b; Chen et al., 2022; Niu et al., 2022). Among them, zeolite, especially ZSM-5, supported noble metal catalysts exhibited the good deep hydrogenation capabilities (Fu et al., 2015; Niu et al., 2022). The acid sites of zeolites can not only modify the dispersion and electric properties of the supported metal species, but also act as active sites for spillover hydrogenation (Lin and Vannice, 1993; Liu et al., 2020b; Lu et al., 2021a, 2021b). Nevertheless, the intrinsic natures of ZSM-5 micropores limit the diffusion of PAHs, resulting in low accessibility and utilization of acid sites. To solve the problem, the introduction of mesopores into ZSM-5 framework has been achieved by various methods, including the framework-etching, alkaline treatment, the direct synthesis of zeolite in the presence of mesopores templating agents (Fu et al., 2016; Li et al., 2017; Peng et al., 2018; Niu et al., 2022; Pan et al., 2024). For example, Wang group (Niu et al., 2022) fabricated hollow ZSM-5 with hierarchical porous structure by alkaline treatment, and the prepared corresponding Pt/ZSM-5 catalysts exhibited good deep hydrogenation capability in the hydrogenation of PAHs. Additionally, Fu et al. (2016) synthesized mesoporous ZSM-5 (ZSM-5-M) in a crystallization system employing a secondary template of quaternary ammonium groups (COPQA), and demonstrated that Ni_2P/ZSM-5-M showed good catalytic performance in both the hydrogenation of PHE and the hydrodesulfurization (HDS) of 4,6-dimethyldibenzothiophene (4,6-DM-DBT). In our previous work, we have demonstrated that mesoporous ZSM-5 synthesized in the absence of the secondary template can serve as an effective catalyst support for the hydrogenation of naphthalene. More significantly, the experimental results revealed that the acidity of ZSM-5 greatly influenced the hydrogenation capability of the prepared Pt/ZSM-5. Furthermore, the acid-induced hydrogenation (spillover hydrogenation) played a dominated role in the hydrogenation of naphthalene over Pt/ZSM-5 (Liu et al., 2020b).

Hydrogenation of PAHs over ZSM-5 supported metal catalysts predominantly occurs on the external surface of ZSM-5, primarily due to its smaller pore size than PAHs. With regard to zeolite-supported noble metal catalysts, PAHs adsorbed on the acid sites of zeolite supports can be hydrogenated through spillover hydrogenation. Thus, the density of acid sites on the external surface of ZSM-5 is a pivotal factor influencing the hydrogenation performance of the supported metal catalysts (He et al., 2013; Liu et al., 2020b; Lu et al., 2021a; Niu et al., 2022). Apart from modifying the Si/Al ratios of ZSM-5 and introducing mesopores into ZSM-5, precisely tailoring the Al_F distribution of ZSM-5 may also serve as an alternative strategy for optimizing hydrogenation performance. However, the influencing mechanism of acidity variations in zeolite supports, arising from the differences in Al_F distribution (including the enrichment degree of Al_F on the internal/external surfaces of the zeolite, Al_F location in the different channels and the arrangement mode of Al_F on the ten-membered rings) on the catalytic behavior of the zeolite-supported metal catalysts in the deep hydrogenation performance of PAHs remains unclear.

In this work, two series of mesoporous ZSM-5 zeolites with the differences in Al_F distribution but similar Si/Al ratios were synthesized in the crystallization system with or without NaOH, and the corresponding supported Pt catalyst were delicately fabricated via impregnation method. Various characterizations and the controlled reactions results demonstrate that the higher enrichment degree of Al_F on the external surface and the suitable arrangement mode of Al_F in ten-membered ring (10-MR) of HZSM-5-F-*x* compared to HZSM-5-E-*x* in case of the similar Si/Al ratios, result in the distinct deep hydrogenation performance of PHE in the fabricated two series of Pt/HZSM-5 catalysts. The purpose of this work is expected to gain insights into the impact of Al_F distribution in ZSM-5 on the deep hydrogenation of PAHs, and to provide theoretical and experimental evidence for design of efficient zeolite-based catalysts for the deep hydrogenation of PAHs under mild reaction conditions.

2. Experimental section

2.1. Materials

Chemicals and reagents, HY (Si/Al = 48) from Sinopec Dalian (Fushun) Petrochemical Research Institute; Hβ (Si/Al = 35) from Tianjin Nankai Catalyst Co. Ltd.; Commercial HZSM-5-com (Si/Al = 30) from Alfa Aesar (China) Chemicals Co. Ltd.; γ-Al_2O_3 and cyclohexane (≥99.0%) from Shanghai Macklin Biochemical Co. Ltd.; SiO_2, Aluminum isopropoxide (IPA, ≥98.0%), chloroplatinic acid ($H_2PtCl_6{\cdot}6H_2O$, 37.5 wt% Pt), tetralin (≥99.5%) and oxalic acid (Anhydrous 98%) from Aladdin Co. Ltd.; Sodium hydroxide (NaOH), tetraethyl orthosilicate (TEOS, ≥98.0%), ethanol (EtOH, ≥99.7%), ammonium nitrate (NH_4NO_3, ≥99.5%) and sodium chloride (NaCl, ≥99.5%) from Tianjin Comio Chemical Reagent Co. Ltd.; Phenanthrene (PHE, ≥99.0%) from Energy Chemistry; Symmetric octahydrophenanthrene (sym-OHP, ≥98.0%) and 1,3,5-triisopropylbenzene (TIPB, ≥95.0%) form TCI; Tetrapropylammonium hydroxide solution (TPAOH, 25 wt% in water) from Innochem. All chemicals were used as received without any purification.

2.2. Catalyst preparation

ZSM-5-F zeolites with different Si/Al molar ratios were synthesized in the system without NaOH according to the reference with some changes (Liu et al., 2020a). The molar compositions of the initial synthesis gel were 1 SiO_2: 0.0033–0.02 Al_2O_3: 0.3 TPAOH: 20 H_2O. For ZSM-5-F-50, IPA (0.41 g) was added to the solution containing deionized water (17.89 g) and TPAOH (24.67 g). The mixture was stirred at room temperature for 12 h before adding TEOS (21.06 g) dropwise. The synthesis gel after stirring for 12 h was transferred into a 100 mL Teflon-lined autoclave and heated at 180 °C for 48 h. The solid products were centrifuged, washed with deionized water repeatedly, and dried overnight at 80 °C. After the dried sample was calcined at 550 °C for 5 h in air, HZSM-5-F-*x* (*x* represents the targeted Si/Al molar ratios) zeolite samples were obtained. ZSM-5-E-*x* with a similar Si/Al ratio to ZSM-5-F-*x* was synthesized in the crystallization system containing NaOH, and HZSM-5-E-*x* was obtained by exchanging calcined ZSM-5-E-*x* with NH_4NO_3 solution (1 mol/L). The detailed synthesis and ion-exchanging procedures were shown in the Supporting Information.

Pt/HZSM-5 catalysts were prepared via wetness impregnation. The procedure was as follows: the required amount of $H_2PtCl_6{\cdot}H_2O$ was dissolved in deionized (20 mL) water, and then HZSM-5-F-*x* or HZSM-5-E-*x* (1 g) was added into it. After the mixture was stirred continuously at 30 °C for 24 h, the solvent was removed by rotary evaporation and the solid product was dried at 70 °C for 8 h. The dried products were calcined at 350 °C for 4 h under air atmosphere, and then reduced with a mixture of H_2/Ar (10% H_2 by volume) at 350 °C for 2 h. The obtained catalysts were recorded as Pt/HZSM-5-F-*x* and Pt/HZSM-5-E-*x*, respectively. Furthermore, the reference samples Pt/γ-Al_2O_3, Pt/SiO_2, Pt/HZSM-5-com, Pt/HY and Pt/Hβ were also prepared according to the above procedure. The Pt loading in the catalyst is 1.0 wt%, unless otherwise specified.

2.3. Characterization

XRD measurement was conducted on an XRD-6000 X-ray diffractometer (Shimadzu, Japan). SEM measurement was carried out on A Hitachi S-4800 scanning electron microscope (Shimadzu, Japan). N_2 adsorption-desorption isotherms was obtained on a NOVA 1200e adsorption analyzer (Quantachrome, USA). High-resolution TEM (HRTEM) images were obtained on a JEM2011 (JEOL) electron microscope. Thermogravimetric-differential scanning calorimetry analysis (TG-DSC) was performed on a NETZSCH STA 449 F3 instrument. X-ray photoelectron spectra (XPS) of platinum containing samples were recorded on a Thermo Scientific ESCALAB 250Xi spectrometer. The temperature-programmed desorption of ammonia/hydrogen (NH_3-TPD/H_2-TPD/H_2-Chemisorption) was acquired on VDSorb-91i. ^{27}Al magic angle spinning nuclear magnetic resonance (MAS NMR) spectra of were performed on a BRUKER AVANCE III 400 MHz spectrometer. Pyridine (Py) and 2,6-ditert-butylpyridine (DTBPy) desorption infrared spectra and were recorded using a Shimadzu IR Affinity-1. The element analysis was carried out on a Thermo iCAP 6300 (Thermo Fisher, USA) inductively coupled plasma atomic emission spectrometer (ICP-AES). The details were described in the Supporting Information.

2.4. Catalytic reaction tests

Hydrogenation of PHE was performed in a 100 mL high-pressure reactor (Anhui-CHEM^N Instrument Co.; Ltd) with a quartz liner. The stirring rate was set to 700 rpm to eliminate the effect of mass transfer (Fig. S1, Supporting Information). For a typical procedure, 0.05 g of catalyst (>300 mesh), 0.10 g of phenanthrene and 20 mL of cyclohexane were added to the reactor and the air in it was repeatedly replaced with H_2 prior to testing. Subsequently, the autoclave was charged with H_2 to the required pressure, as the temperature was close to the set value. The autoclave was cooled immediately after the completion of the reaction. The reaction products were analyzed on an Agilent 7820A gas chromatograph equipped with an HP-5 capillary column (30 m × 0.25 mm × 0.25 μm).

2.5. Computations

The details of all density functional theory (DFT) calculations were given in Supporting Information.

3. Results and discussion

3.1. Physicochemical properties of HZSM-5-F-x and HZSM-5-E-x

Two series of HZSM-5 samples, HZSM-5-F-*x* and HZSM-5-E-*x*, were synthesized in a similar synthesis system, varying in the absence or presence of a small amount of NaOH. As shown in Fig. 1(a) and Fig. S2, the XRD patterns of HZSM-5-F-*x* and HZSM-5-E-*x* samples show the typical MFI characteristic diffraction peaks (JCPDS No.42-0024) at $2\theta = 7.9°$, 8.8°, 23.1°, 23.8° and 24.4° (Zhang et al., 2019a), although HZSM-5-E-*x* demonstrates slightly higher crystallinity than HZSM-5-F-*x*.

SEM images and particle sizes distribution of HZSM-5-F-*x* and HZSM-5-E-*x* samples are displayed in Figs. S3–S4. As illustrated in Figs. S3–S4, HZSM-5-F-*x* and HZSM-5-E-*x* exhibit similar morphology and uniform particle size distribution. The average particle sizes of two series of HZSM-5 samples are within the span of 213–299 nm.

The N_2 adsorption-desorption isotherms in Fig. 1(b) and Fig. S5 indicates that the two series of HZSM-5 samples exhibit a sharp uptake at $p/p_0 < 0.02$, implying their microporous natures. In addition, their N_2 adsorption-desorption isotherms show hysteresis loops at a high relative pressure range of 0.8–0.95, although the hysteresis loop observed for HZSM-5-F-*x* is more pronounced than HZSM-5-E-*x*. This is related to the adsorption of N_2 in the inter-crystalline voids formed by stacking of the nano-sized crystals (Cychosz et al., 2017; Yang et al., 2017; Ma et al., 2023). The composition and textural properties of the fabricated samples are depicted in Table 1. As shown in Table 1, the surface areas and pore volumes of HZSM-5-F-*x* and HZSM-5-E-*x* samples are comparable. Furthermore, the result of ICP measurement demonstrates the similar Si/Al ratios for HZSM-5-F-*x* and HZSM-5-E-*x* samples.

^{27}Al MAS NMR analysis (Fig. 1(c) and Fig. S6) shows that the two series of HZSM-5 samples exhibit a dominant signal peak centered at 54 ppm and a weak peak centered at 0 ppm, which can be ascribed to framework tetrahedrally coordinated Al and extra-framework octahedral Al, respectively. Evaluation of relative intensities of the two peaks (Table S1) indicates that the Al species of two HZSM-5-F-*x* and HZSM-5-E-*x* samples predominantly exist as the form of framework tetrahedrally coordinated Al (Al_F). The broad peak centered at 54 ppm (ranging from 45 to 65 ppm) ascribed to Al_F species in HZSM-5-F-*x* and HZSM-5-E-*x* samples was deconvoluted into four peaks at 52, 54, 56, and 58 ppm, respectively (Fig. 1(c)–(e) and Fig. S6). The relative proportions of these peaks were given in Table S1. In general, the peak at 54 ppm is attributed to Al_F species at the intersection of the straight and sinusoidal, whereas the peak at 56 ppm is associated with Al_F species in the straight or sinusoidal (Yokoi et al., 2015; Liang et al., 2016; Wang et al., 2018; Guo et al., 2024). As shown in Fig. 1(c)–(e), Fig. S6 and Table S1, the ratio of 54/56 ppm for HZSM-5-F-50 (1.2) is lower than HZSM-5-E-50 (2.0), indicating that the proportion of Al_F species within the straight or sinusoidal in HZSM-5-F-50 is higher than that of HZSM-5-E-50. Similar results were also observed for the two series of HZSM-5 samples with different Si/Al ratios, namely, HZSM-5-F-80/150 and HZSM-5-E-80/150 (Fig. S6 and Table S1). Although it is difficult to precisely locate and assign Al_F to the specified T-sites using NMR chemical shifts, it is a useful tool for obtaining information on the distribution of Al_F at various T-sites.

In addition, the proportions of single Al and Al pairs, as well as their distribution in HZSM-5-F-50 and HZSM-5-E-50**,** were estimated using exchanged Co^{2+} cations as a probe (Dědeček et al., 2000; Liang et al., 2016; Guo et al., 2024; Wang et al., 2024). The quantitative results for single Al and Al pairs are summarized in Table S2. Upon deconvolution of the UV–vis-DRS spectra of Co-ZSM-5-F-50 and Co-ZSM-5-E-50 using a Gaussian function (Fig. S7 and Table S2), seven distinct bands were revealed. These bands can be sorted into three types of Co(II) ions coordinated with different Al T-sites: α-type Co(II) ions in the straight channel represented by a single band at 15,100 cm^{-1}; β-type Co(II) ions in the channel intersections, characterized by four bands at 16,000, 17,150, 18,600, and 21,200 cm^{-1}; and γ-type Co(II) ions in the sinusoidal channels,

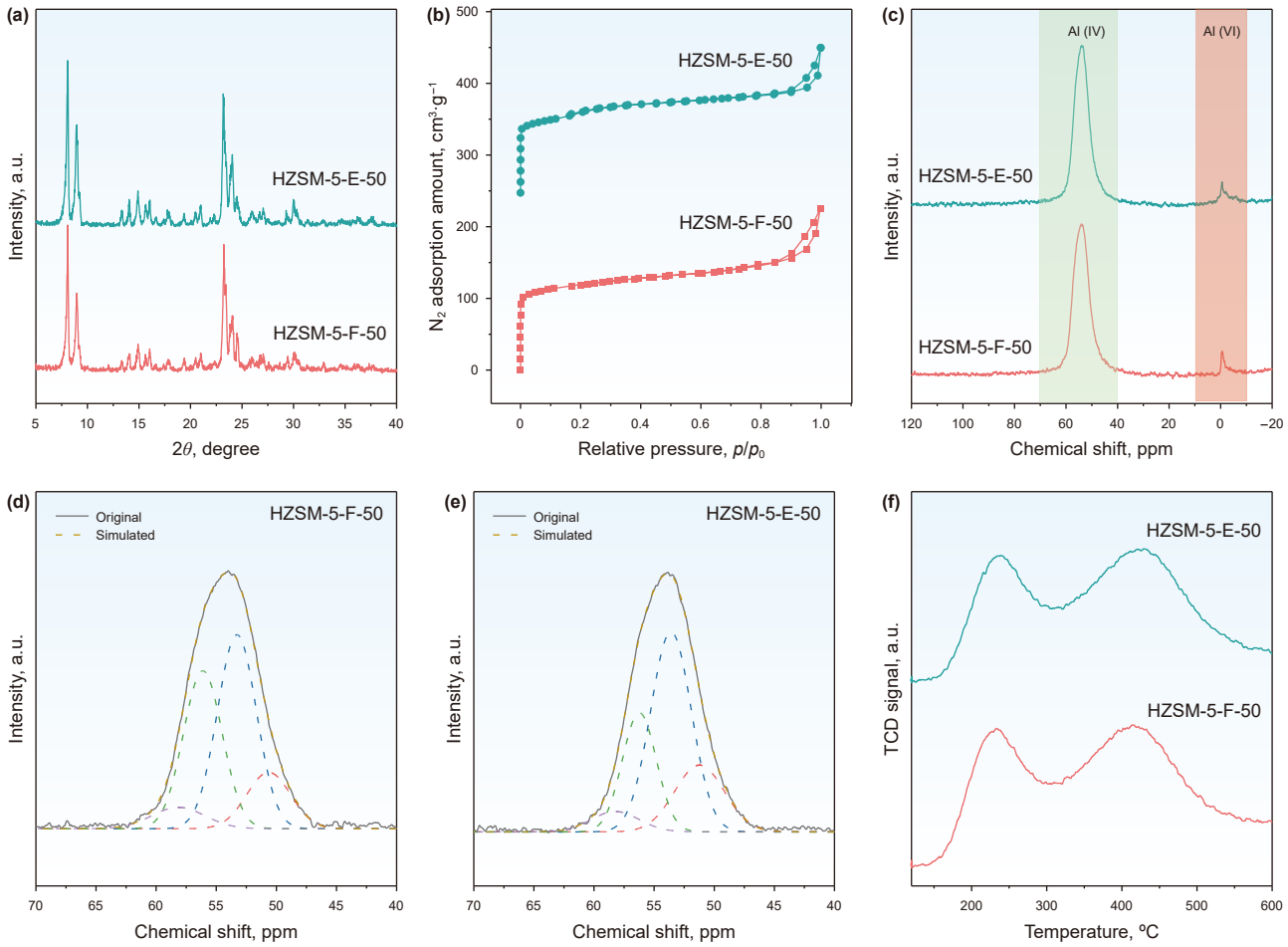

Fig. 1. (**a**) Powder XRD patterns, (**b**) N_2 adsorption-desorption isotherms, (**c**) ^{27}Al MAS NMR spectra, (**d**) and (**e**) deconvolution of the ^{27}Al MAS NMR spectra, (**f**) NH_3-TPD curves of HZSM-5-F-50 and HZSM-5-E-50.

Table 1
The textural properties and chemical composition of different samples.

Sample	S_{BET}, m^2/g[a]	S_{mic}, m^2/g[b]	S_{ext}, m^2/g[b]	V_{mic}, cm^3/g[b]	V_{mes}, cm^3/g[c]	Si/Al[d]	Si/Al[e]
HZSM-5-F-50	382	290	92	0.14	0.19	51.3	23.8
HZSM-5-E-50	376	277	99	0.14	0.17	52.9	36.0
HZSM-5-F-80	375	295	80	0.15	0.17	70.0	33.8
HZSM-5-E-80	401	312	89	0.15	0.15	71.3	46.5
HZSM-5-F-150	392	313	79	0.16	0.18	129.0	73.5
HZSM-5-E-150	380	298	82	0.15	0.17	134.3	82.3

[a] Determined by the BET method.
[b] Calculated by t-plot.
[c] Derived by the DFT method from the adsorption branches of the isotherms.
[d] Determined by ICP.
[e] Determined by XPS.

associated with the bands at 20,100 and 22,000 cm^{-1}. The distribution proportions of the Al pairs are also listed in Table S2. Notably, the proportions of single Al, Al pairs, and the distribution of Al pairs in HZSM-5-F-50 and HZSM-5-E-50 are comparable.

The NH_3-TPD analysis of HZSM-5-F-*x* and HZSM-5-E-*x* samples (Fig. 1(f), Fig. S8 and Table 2), along with the Py-IR characterization for two representative samples, HZSM-5-F-50 and HZSM-5-E-50 (Table 3), show that the acidity of the two series of HZSM-5-F-*x* and HZSM-5-E-*x* samples is comparable.

ICP measurements show that the two series of HZSM-5 samples have similar bulk Si/Al ratios in Table 1. However, their surface Si/Al ratios measured by XPS are significantly lower than their bulk Si/Al ratios, indicating the enrichment of Al_F species on their external surface (Table 1). Moreover, the enrichment degree of Al_F on the external surface of HZSM-5-F-*x* is higher than HZSM-5-E-*x*, which is further confirmed by the results of catalytic cracking of TIPB and DTBPy-IR.

The size of TIPB (0.95 nm) is larger than the pore size of ZSM-5, thus, the catalytic cracking results of TIPB over HZSM-5 can reflect the Brønsted acid amounts on its external surface (Mensah et al., 2021; Zhao et al., 2021). As expected, the conversion of TIPB over HZSM-5-F-*x* surpasses that over HZSM-5-E-*x* under the identical

Table 2
The acidity of HZSM-5-F-*x* and HZSM-5-E-*x* samples.

Sample	Acidity by NH_3-TPD, μmol/g[a]		
	Total	Weak	Strong
HZSM-5-F-50	285.4	67.7	217.7
HZSM-5-E-50	281.0	62.5	218.5
HZSM-5-F-80	253.8	52.6	201.2
HZSM-5-E-80	240.3	49.6	190.7
HZSM-5-F-150	133.2	20.7	112.5
HZSM-5-E-150	125.5	18.5	107.0

[a] The amounts of weak and strong acid were measured by the amounts of ammonia desorbed at 120–300 °C and 300–550 °C, respectively.

Table 3
The acidity of different samples.

Sample	Acidity by Py-IR, μmol/g[a]			Acidity by DTBPy-IR, μmol/g[b]
	Total	Lewis	Brönsted	external Brønsted
HZSM-5-F-50	87.5	28.0	59.5	19.5
HZSM-5-E-50	80.8	25.9	54.9	10.4

[a] The amounts of Brønsted and Lewis acid were calculated from the Py-IR spectra at 150 °C.
[b] The amounts of external Brønsted acid were determined by DTBPy-IR spectra at 150 °C.

reaction conditions (Table S3). The kinetic diameter of DTBPy exceeds the pore size of ZSM-5 (0.56 nm), restricting its diffusion into the micropores. Thus, DTBPy adsorption amounts on ZSM-5 can serve as a reliable indicator for evaluating the Brønsted acid amounts on its external surface (Góra-Marek et al., 2014). To further clarify the different enrichment degree of Al_F on the external surface of the two series HZSM-5 samples, two representative samples, HZSM-5-F-50 and HZSM-5-E-50, were selected to perform DTBPy-IR measurement. As shown in Table 3, the Brønsted acid amounts detected on the external surface of HZSM-5-F-50 is higher than that on HZSM-5-E-50.

In zeolite synthesis, nucleation initiates at the early stage. Silica units are more preferentially incorporated into the initial nuclei compared to aluminum species (Thompson, 1992). As the depolymerization-polymerization process progresses, the soluble silicate species are gradually depleted, and then aluminum-rich soluble species are gradually incorporated into the outer layers of the growing particles. This is the known mechanism and also the main reason for the inhomogeneous Al distribution in zeolite crystals (mainly during the induction period) (Derouane et al., 1981; Serrano et al., 2001). In this work, the different Al_F distribution in the two series of HZSM-5 samples are closely related to their synthesis system. In the synthesis system without NaOH, AlO_4^- can be only balanced by TPA^+, thus, AlO_4^- locates at the vicinity of the part of TPA^+. In contrast, in the synthesis system containing NaOH, AlO_4^- can be balanced by Na^+ or TPA^+, thus AlO_4^- locates at any framework T-site, not just in the vicinity of TPA^+, which results in a wider dispersion of Al species in zeolite framework (Dedecek et al., 2012; Dědeček et al., 2019).

3.2. Physicochemical properties of HZSM-5-F-x or HZSM-5-E-x supported Pt catalysts

The XRD patterns in Fig. 2(a) and Fig. S2 display that the two series of Pt/HZSM-5 catalysts (Pt/HZSM-5-F-*x* and Pt/HZSM-5-F-*x*) also basically maintain the crystallinity of their corresponding supports, and no additional diffraction peaks corresponding to Pt species are detected, which may be attributed to the high dispersion of Pt and low Pt loading in the two series of catalysts (Song et al., 2019). The two series of Pt/HZSM-5 catalysts keep the morphology and the particle sizes of their corresponding supports, as shown in SEM images (Fig. S3). The results of N_2 adsorption-desorption (Fig. 2(b), Fig. S5 and Table 4) indicate that Pt/HZSM-5-F-*x* and Pt/HZSM-5-E-*x* catalysts exhibit the similar isotherms to their corresponding supports. A slight reduction on the surface area and pore volume is observed on Pt/HZSM-5-F-*x* and Pt/HZSM-5-E-*x* in comparison with HZSM-5-F-*x* and HZSM-5-E-*x*.

The dispersion and electronic states of the supported Pt species on the two series of catalysts were investigated over two representative samples, Pt/HZSM-5-F-50 and Pt/HZSM-5-E-50. As shown in Fig. 2(c), the Pt NPs in Pt/HZSM-5-F-50 and Pt/HZSM-5-E-50 are about 2.1 and 3.1 nm in size, respectively. This is basically consistent with the results of H_2 chemisorption (Table 4). As the Pt NPs are much larger than the channel size of ZSM-5, most of the Pt species on the Pt/HZSM-5-F-50 and Pt/HZSM-5-E-50 catalysts are mainly located on the external surface of HZSM-5 support.

The Pt 4f XPS spectra for Pt/HZSM-5-F-50 and Pt/HZSM-5-E-50 are illustrated in Fig. 2(d). Since the XPS spectrum of Pt $4f_{5/2}$ overlaps with that of Al 2p, thus, the XPS spectra of Pt $4f_{7/2}$ were selected to investigate the electronic states of Pt species. As displayed in Fig. 2(d), the binding energies of the Pt $4f_{7/2}$ peak over Pt/HZSM-5-F-50 and Pt/HZSM-5-E-50 are at 71.4 eV and 71.2 eV, respectively, which are higher than 71.0 eV (Pt^0 species), indicating the presence of partially electron-deficient Pt species in the two Pt/HZSM-5 catalysts. This could be attributed to the electron transfer from Pt to ZSM-5 support, which is in agreement with that reported in the literature (Kubička et al., 2006). Moreover, compared with Pt/HZSM-5-E-50, the binding energy of Pt $4f_{7/2}$ on Pt/HZSM-5-F-50 is shifted towards higher binding energy (around 0.2 eV), which is associated with the stronger interaction between the Pt species and support in Pt/HZSM-5-F-50 (Niu et al., 2022).

The H_2-TPD profiles of Pt/HZSM-5-F-50 and Pt/HZSM-5-E-50 catalysts are shown in Fig. 2(e). As shown in Fig. 2(e), the Pt/HZSM-5-F-50 and Pt/HZSM-5-E-50 catalysts exhibit two H_2 desorption peaks, in which the desorption peaks at low temperatures are mainly attributed to the desorption of H_2 chemisorbed on metal Pt species, while the desorption peaks at high temperatures are associated with the desorption of spillover hydrogen (Miller et al., 1993). However, the peak areas of Pt/HZSM-5-F-50 at high temperature are much larger than Pt/HZSM-5-E-50, implying that the spillover hydrogen on Pt/HZSM-5-F-50 is more than that on Pt/HZSM-5-E-50. This phenomenon can likely be attributed to the combination of its smaller Pt particle size and the presence of a greater number of acid sites in close proximity to the active metal species (Prins, 2012; Niu et al., 2022).

3.3. Catalytic performances

Hydrogenation of phenanthrene (PHE) is a consecutive reaction, and the main products include 9,10-dihydrophenanthrene (DHP), 1,2,3,4-tetrahydrophenanthrene (THP), and deep hydrogenation products (DHPS, symmetric and asymmetric octahydrophenanthrene (sym/asym-OHP) and perhydrophenanthrene (PHP)) (Fu et al., 2015, 2019).

The conversion of PHE and product selectivity of various catalysts are summarized in Table 5. As shown in Table 5, no substrate conversion was observed in the absence of catalyst or in the presence of HZSM-5-F-*x* and HZSM-5-E-*x* samples (Entries 1–3) under the employed reaction conditions. In contrast, the Pt/HZSM-5-F-*x* and Pt/HZSM-5-E-*x* catalysts exhibited significant hydrogenation performance for PHE, indicating that the supported Pt species are indispensable for its hydrogenation. However, Pt/HZSM-5-F-*x* showed a much higher conversion of PHE than Pt/HZSM-5-E-*x* at a reaction time of 20 min (Entries 4–9). Upon prolonging the reaction

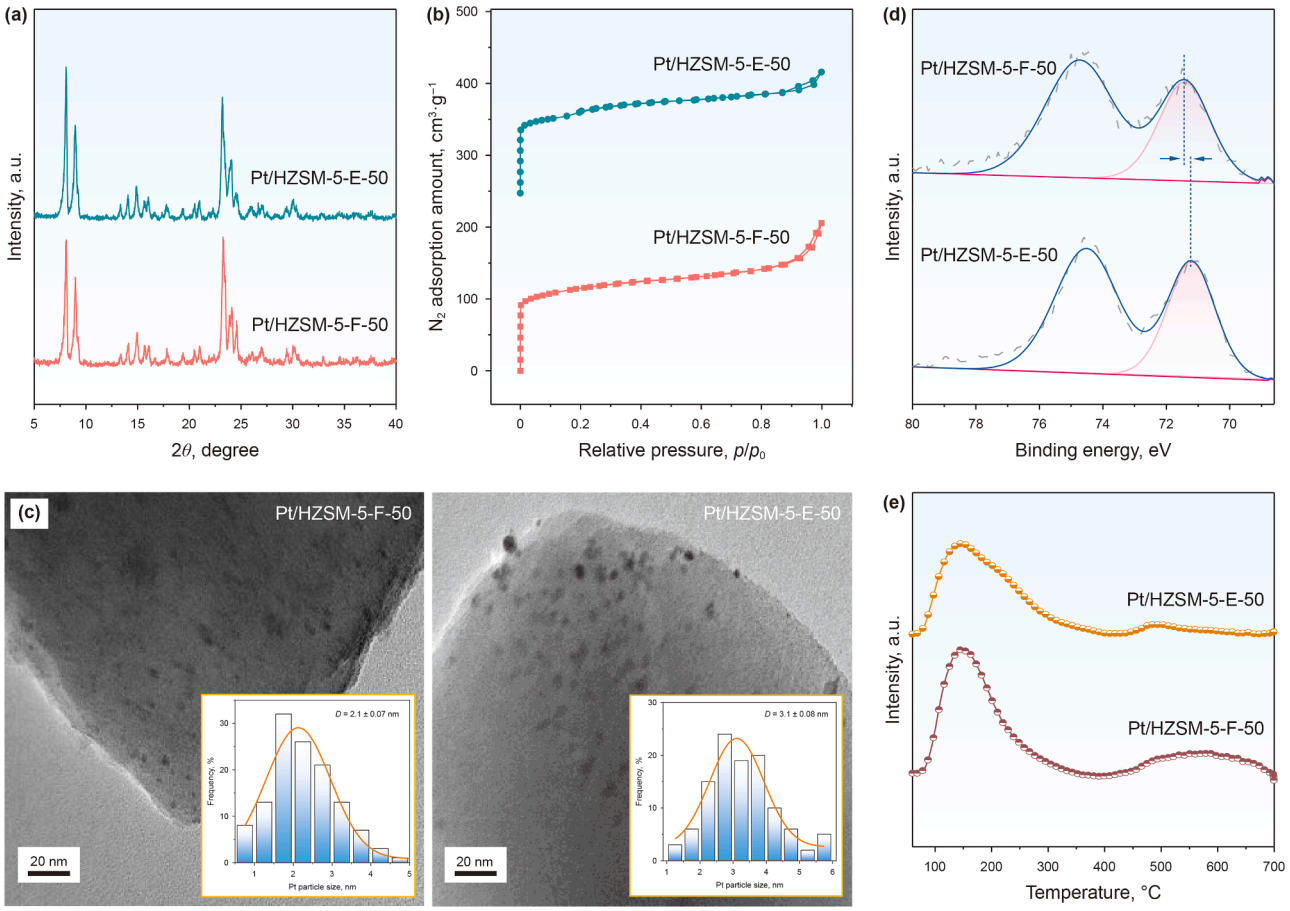

Fig. 2. **(a)** Powder XRD patterns, **(b)** N_2 adsorption-desorption isotherms, **(c)** HRTEM images (the insert pattern of HRTEM images is the particle size distribution of Pt NPs), **(d)** Pt 4f XPS spectra, **(e)** H_2-TPD profiles of Pt/HZSM-5-F-50 and Pt/HZSM-5-E-50.

Table 4
The textural properties and chemical composition of different catalysts.

Sample	S_{BET}, m^2/g[a]	S_{mic}, m^2/g[b]	S_{ext}, m^2/g[b]	V_{mic}, cm^3/g[b]	V_{mes}, cm^3/g[c]	Pt dispersion, %[d]
Pt/HZSM-5-F-50	374	285	89	0.14	0.17	51.6
Pt/HZSM-5-E-50	365	270	95	0.13	0.15	47.9
Pt/HZSM-5-F-80	353	277	76	0.14	0.15	49.2
Pt/HZSM-5-E-80	376	295	81	0.15	0.12	46.8
Pt/HZSM-5-F-150	373	307	66	0.15	0.15	43.8
Pt/HZSM-5-E-150	359	282	77	0.15	0.14	41.6

[a] Determined by the BET method.
[b] Calculated by t-plot.
[c] Derived by the DFT method from the adsorption branches of the isotherms.
[d] Determined by H_2 chemisorption.

time to 10 h, the conversions of PHE over the two series of catalyst were above >99.0%, and the selectivity of PHP obtained over Pt/HZSM-5-F-*x* was also higher than that over Pt/HZSM-5-E-*x* (Entries 10–15). These results indicate that Pt/HZSM-5-F-*x* has a stronger hydrogenation capability than the corresponding Pt/HZSM-5-E-*x*. In addition, for Pt/HZSM-5-F-50/80/150 and/or Pt/HZSM-5-E-50/80/150, their selectivity of PHP decreased with the Si/Al ratios, respectively. The different hydrogenation capability of PHE exhibited by the two series of catalysts can be further demonstrated by the effects of the reaction temperature on their catalytic performance over Pt/HZSM-5-F-50 and Pt/HZSM-5-E-50 (Fig. 3 and Fig. S9). At 200 °C, Pt/HZSM-5-F-50 exhibited nearly complete conversion of PHE (>99.0%), yielding 78.0% deep hydrogenation products, specifically 48.3% sym-OHP, 22.3% asym-OHP and 7.4% PHP. In contrast, Pt/HZSM-5-E-50 only achieved a 74.1% conversion of PHE with DHP being the predominate products (53.1%). As the reaction temperature increased to 220 °C, the conversions of PHE over the two catalysts approached near-complete conversion. However, the selectivity to deep hydrogenation products over Pt/HZSM-5-E-50 was only 68.3%, as opposed to nearly 100% over Pt/HZSM-5-F-50. At 250 °C, the selectivity to PHP over Pt/HZSM-5-F-50 reached 99.2%, while that over Pt/HZSM-5-E-50 was only 44.5%. At 270 °C, the selectivity of PHP over Pt/HZSM-5-F-50 slightly decreased. Concurrently, sym-OHP amount increased, and small amounts of DHP and asym-OHP were detected. This can be attributed to that the high reaction temperature is conducive to the inverse reaction, which is consistent with that reported in the literatures (Pinilla et al., 2014; Liu et al., 2018).

Table 5
Conversion of PHE and product selectivity of different catalysts.

Entry	Sample	Reaction time	Conversion, %	Selectivity, %				
				DHP	THP	sym-OHP	asym-OHP	PHP
1	Blank	10 h	–					
2	HZSM-5-F-*x*	10 h	–					
3	HZSM-5-E-*x*	10 h	–					
4	Pt/HZSM-5-F-50	20 min	70.6	51.7	16.8	25.9	5.6	–
5	Pt/HZSM-5-E-50	20 min	27.8	59.6	31.9	8.5	–	–
6	Pt/HZSM-5-F-80	20 min	39.2	53.7	29.8	14.5	2.0	–
7	Pt/HZSM-5-E-80	20 min	24.1	60.0	32.2	7.8		
8	Pt/HZSM-5-F-150	20 min	23.6	59.8	32.9	7.3	–	–
9	Pt/HZSM-5-E-150	20 min	16.5	53.1	40.7	6.2	–	–
10	Pt/HZSM-5-F-50	10 h	>99.0	–	–	0.8	–	99.2
11	Pt/HZSM-5-E-50	10 h	>99.0	–	–	45.7	9.8	44.5
12	Pt/HZSM-5-F-80	10 h	>99.0	–	–	38.5	4.8	56.7
13	Pt/HZSM-5-E-80	10 h	>99.0	–	–	60.4	8.8	30.8
14	Pt/HZSM-5-F-150	10 h	>99.0	–	–	60.3	10.9	28.8
15	Pt/HZSM-5-E-150	10 h	>99.0	–	–	70.6	13.2	16.2

Reaction conditions: 0.05 g catalyst, 0.1 g phenanthrene, 20 mL cyclohexane, 3 MPa H_2, $T = 250$ °C.

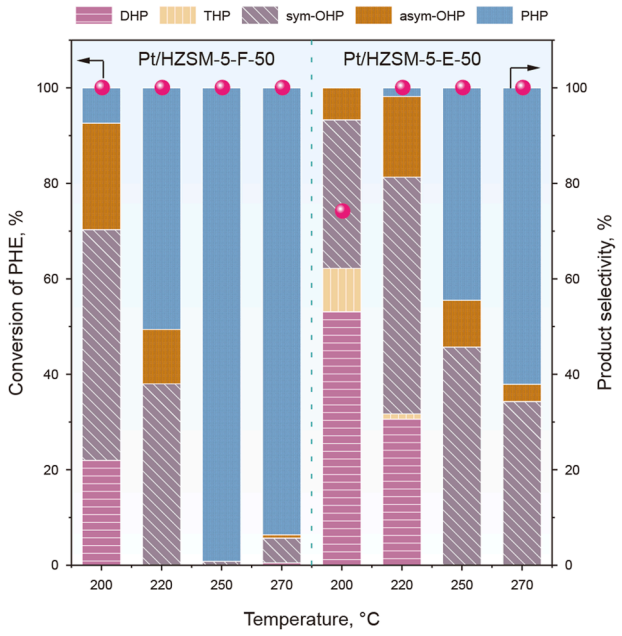

Fig. 3. Conversion of PHE and product selectivity over Pt/HZSM-5-E-50 and Pt/HZSM-5-F-50 at different reaction temperature. Reaction conditions: 0.05 g catalyst, 0.1 g phenanthrene, 20 mL cyclohexane, 3 MPa H_2, $t = 10$ h, $T = 200$–270 °C.

3.4. Discussion on the different hydrogenation performance of Pt/HZSM-5-F-50 and Pt/HZSM-5-E-50

Acidic zeolite-supported metal catalysts typically give an enhanced hydrogenation performance compared to other inert support supported metal catalysts (Liu et al., 2020b; Lu et al., 2021a). The enhanced catalytic performance can be primarily attributed to additional spillover hydrogenation (acid-induced hydrogenation). Therefore, the hydrogenation performance of PHE over Pt/HZSM-5 is closely related to its metal hydrogenation and spillover hydrogenation capabilities. Compared to Pt/HZSM-5-E-50, Pt/HZSM-5-F-50 has a higher Pt dispersion as evidenced by TEM measurement, thus the differences of the two catalysts in the metal dispersion may result in their distinct hydrogenation capability. For eliminating the influence of spillover hydrogenation, the corresponding Pt/NaZSM-5-F-50 and Pt/NaZSM-5-E-50 catalysts were prepared by exchanging Pt/HZSM-5-F-50 and Pt/HZSM-5-E-50 through ion-exchange with 1 mol/L NaCl solution, respectively. NH_3-TPD results revealed that the strong acid sites detected on NaZSM-5 were less than HZSM-5 (Fig. S10). However, Pt/NaZSM-5-F-50 and Pt/NaZSM-5-E-50 catalysts, as shown in Table S4, exhibited nearly similar catalytic performance in term of both conversion of PHE and product selectivity. Thus, the difference of Pt dispersion between the two Pt/HZSM-5 catalysts is insufficient to account for their markedly distinct deep hydrogenation capacity for PHE. Additionally, the main products obtained over Pt/NaZSM-5-F-50 and Pt/NaZSM-5-E-50 were partial hydrogenation products, with significantly less complete hydrogenation product (PHP) compared to their corresponding Pt/HZSM-5 catalysts. The above results indicate that spillover hydrogenation induced by strong acid sites plays a pivotal role in facilitating hydrogenation of PHE to PHP.

Spillover hydrogenation involves the migration of activated hydrogen species formed on the metal sites to adjacent acid sites within the metal-acid interfacial region, where the reactants adsorbed on acid sites can be hydrogenated by the active hydrogen species. Thus, the amounts of acid sites with a close proximity to the metal sites plays a crucial role in hydrogenation reaction. The hydrogenation of PHE over Pt/HZSM-5 primarily occurs on the external surface of HZSM-5, as the kinetic size of PHE (around 0.70 nm) is much larger than the pore size of ZSM-5 (around 0.56 nm) and the supported Pt species are mainly located on the external surface of ZSM-5 (Fig. 2(c)). Thus, combined with the characterization and catalytic results, it is reasonable to infer that the acidity differences on the external surface of HZSM-5-F-*x* and HZSM-5-E-*x* result in the different catalytic hydrogenation capability of PHE between Pt/HZSM-5-F-*x* and Pt/HZSM-5-E-*x*.

To decipher the dependence of PHE hydrogenation performance on the amounts of acid sites on the external surface of HZSM-5 supports, HZSM-5-F-150-oxalic was fabricated by treating HZSM-5-F-150 with oxalic acid solution, which can selectively extract Al species from the external surface (Huang et al., 2016; Yuan et al., 2022). The characterization results of XRD, N_2 adsorption-desorption, NH_3-TPD, DTBPy-IR, ICP and XPS of HZSM-5-F-150-oxalic, along with the corresponding description of HZSM-5-F-150-oxalic, are presented in Supporting Information (Fig. S11; Table S3 and Table S5). The effective removal of acid sites on the external surface of HZSM-5-F-150 through oxalic acid solution treatment can be confirmed by the increased Si/Al ratios detected by XPS, the corresponding reduction in TIPB cracking activity and the results of DTBPy-IR (Table S3 and Table S5). From Fig. S11(c)–(d), it can be observed that the conversion of PHE

showed positive correlation with the amounts of acid sites on the external surface of HZSM-5 supports, while there was no correlation with the total amounts of acid sites.

To further confirm this, a commercial HZSM-5-com with similar textural properties to HZSM-5-F-50, but a higher acid density was used as the reference catalyst for comparison (Table 2, Fig. S12 and Tables S6–S7). The results of catalytic cracking of XPS and TIPB indicate that HZSM-5-com has a lower surface Si/Al ratio, higher catalytic cracking activity than HZSM-5-F-50 (Table S3 and Table S6), suggesting the presence of more acid sites on its external surface, which is in lined with the results of DTBPy-IR (Table S7). In addition, the Pt dispersion of Pt/HZSM-5-com and Pt/HZSM-5-F-50 was 55.7% and 51.6%, respectively, thus, the two catalysts were still comparable in terms of Pt dispersion. However, Pt/HZSM-5-F-50 (70.6%) showed a higher conversion of PHE than Pt/HZSM-5-com (61.9%) at a reaction time of 20 min. Upon prolonging the reaction time to 6 h, the selectivity of PHP obtained over Pt/HZSM-5-com was just 41.1%, lower than that over Pt/HZSM-5-F-50 (63.9%) under the identical reaction conditions. This indicates that the variation in the acid amount on the external surface of HZSM-5-F-50 and HZSM-5-E-50 is not the exclusive factor determining their PHE deep hydrogenation capabilities.

For saturation hydrogenation of PHE, the rate-determining step is the conversion of sym-OHP to PHP, primarily due to steric hindrance in the adsorption of sym-OHP on the catalyst surface and competitive adsorption with partially hydrogenated aromatics (Fu et al., 2015; Wang et al., 2019). Therefore, tetralin with reduced steric hindrance was selected as the substrate. As shown in Table S8, even if Pt/HZSM-5-F-50 still exhibited higher hydrogenation activity than Pt/HZSM-5-E-50 in tetralin hydrogenation, but the differences between the two catalysts were less obvious than that detected in sym-OHP hydrogenation (Table S9). Considering the steric hindrance in the adsorption of sym-OHP on the catalyst surface and the above experimental results, it is reasonable to infer that the Al_F location in ZSM-5 may also influence the deep hydrogenation performance of the prepared Pt/HZSM-5 for PHE.

In order to gain more insights into the relationship between Al_F location and catalytic performance, the adsorption energy of sym-OHP on HZSM-5 was calculated by DFT due to that sym-OHP hydrogenation is the rate-determining reaction step in the deep hydrogenation of PHE to PHP. Based on previous literature (Dědeček et al., 2009, 2019), four different potential slabs were constructed on the representative sample, HZSM-5-50, which contains approximately two Al atoms per unit cell, 1) Al–O–Si–O–Si–O–Al sequences in which Al_F is located in the six-membered ring separated by two Si (Al_{paired}/2Si); 2) Al–O–Si–O–Si–O–Al sequences in which Al_F is located in a different ring separated by two Si ($Al_{unpaired}$/2Si); 3) Al–O–Si–O–Si–O–Si–O–Al sequences separated by three Si ($Al_{unpaired}$/3Si); and 4) acid sites separated by more than three Si (Al_{single}/>3Si). In addition, the Al–O–Si–O–Al sequence is not analyzed due to its negligible probability in zeolites with Si/Al > 8 (Dědeček et al., 2011). The adsorption energies and configurations of sym-OHP on the slabs constructed on HZSM-5-50 are shown in Fig. 4 and Fig. S13. As illustrated in Fig. 4, the order of adsorption energy of sym-OHP on the different constructed slabs is as follows, (Al_{paired}/2Si) > ($Al_{unpaired}$/2Si) > (Al_{single}/>3Si) > ($Al_{unpaired}$/3Si), indicating that the Al_F location has a great influence on the adsorption of sym-OHP on HZSM-5. The Al_F species on the ten-membered ring are more favorable for adsorption of sym-OHP than those on the six-membered ring, in which $Al_{unpaired}$/3Si in the ten-membered ring is the most favorable arrangement mode for adsorption of sym-OHP. The ^{27}Al MAS NMR spectra have revealed that the proportion of Al_F species within the straight or sinusoidal channels in HZSM-5-F-*x* is higher than that in HZSM-5-E-*x*. Consequently, the probability of AlF species on the ten-membered ring in HZSM-5-F-*x* is higher than in HZSM-5-E-*x* in case of the similar Si/Al ratio. Thus, it is reasonable to conclude that the Al_F location is also a crucial factor for two Pt/HZSM-5 catalysts with the difference in deep hydrogenation capabilities of PHE.

Hence, combined with the results of the characterization, experiment and DFT calculation, it can be deduced that the difference in deep hydrogenation capability of PHE is related to the enrichment degree of Al_F on the external surface and Al_F arrangement mode in ten-membered ring in HZSM-5 in case of the similar Si/Al ratios.

Sym-OHP hydrogenation is the rate-determining reaction step in the deep hydrogenation of PHE to PHP (Fig. S14). Thus, to further elucidate the influence of Al_F distribution on the catalytic behavior of Pt/HZSM-5-F-*x* and Pt/HZSM-5-E-*x* in the deep hydrogenation

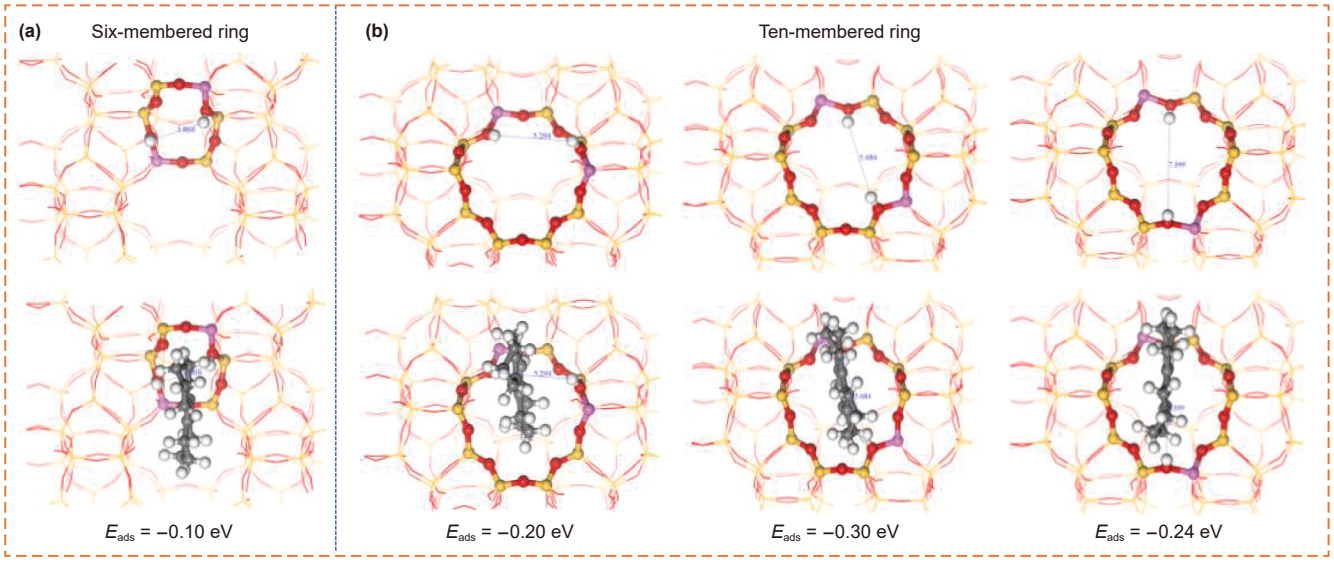

Fig. 4. Computation of sym-OHP adsorption energy in HZSM-5-50 zeolite, **(a)** six-membered ring, **(b)** ten-membered ring. Atomic coloring, Si (yellow), Al (pink), O (red) and H (white).

Table 6
Conversion of PHE and product selectivity of different catalysts.

Entry	Sample	Conversion, %	DHP	Selectivity, %					Others
				THP	sym-OHP	sym-OHA	asym-OHP	PHP	
1	Pt/SiO_2	14.7	52.6	42.5	4.9	–	–	–	–
2	$Pt/\gamma\text{-}Al_2O_3$	16.6	51.4	42.1	6.5	–	–	–	–
3	Pt/HY	71.3	25.0	11.5	19.2	23.7	15.5	3.5	1.6
4	Pt/Hβ	61.7	45.8	19.5	14.3	15.1	5.3		
5	Pt/HZSM-5-F-50	70.6	51.7	16.8	25.9	–	5.6	–	–
6	Pt/HZSM-5-E-50	27.8	59.6	31.9	8.5	–	–	–	–

Reaction conditions: 0.05 g catalyst, 0.1 g phenanthrene, 20 mL cyclohexane, 3 MPa H_2, t = 20 min, T = 250 °C.

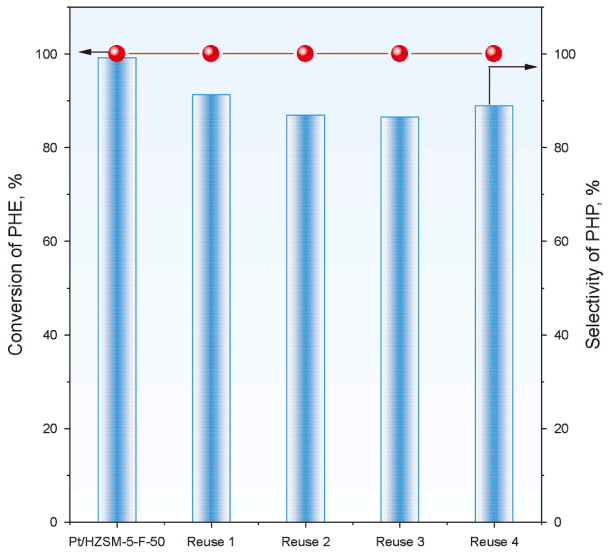

Fig. 5. Reusability of Pt/HZSM-5-F-50 for the conversion of PHE. Reaction conditions: 0.05 g catalyst, 0.1 g phenanthrene, 20 mL cyclohexane, 3 MPa H_2, t = 10 h, T = 250 °C.

performance of PHE, the conversion of sym-OHP was investigated over two representative samples, Pt/HZSM-5-F-50 and Pt/HZSM-5-E-50. As shown in Fig. S14, the apparent activation energy (E_a) of sym-OHP hydrogenation was calculated using the Arrhenius equation based on the reaction rates measured at different temperatures. The calculated E_a values for Pt/HZSM-5-F-50 and Pt/HZSM-5-E-50 were 71.7 and 107.1 kJ/mol, respectively.

To further highlight the properties of Pt/HZSM-5-F-50 for the deep hydrogenation of PHE, a series of supported Pt catalysts were prepared and their hydrogenation performance were compared. As shown in Table 6, compared to Pt/SiO_2 and $Pt/\gamma\text{-}Al_2O_3$ (Entries 1–2), zeolite-supported Pt catalysts exhibited higher hydrogenation performance, as evidenced by the higher conversion of PHE (Entries 3–6). However, zeolite-supported Pt catalysts with various topologies exhibited the distinct hydrogenation performance of PHE. Pt/HZSM-5-F-50 exhibited higher hydrogenation performance of PHE than Pt/Hβ. Although the comparable hydrogenation performance of PHE was observed between Pt/HZSM-5-F-50 and Pt/HY, the cracking products were detected over the latter catalyst (Entries 3–5), even if HY, Hβ and HZSM-5-F-50 are comparable in terms of the strong acid amounts (Fig. S15).

In addition, the catalytic result over Pt/HZSM-5-F-50 for hydrogenation of PHE are compared with previously reported catalysts (Table S10), As shown in Table S10, Pt/HZSM-5-F-50 showed superior deep hydrogenation performance under relatively mild reaction conditions. However, it should be noted that the direct comparison is limited due to differences in hydrogenation reactors and reaction solvent.

3.5. Reusability and parameter optimization for the conversion of PHE over Pt/HZSM-5-F-50

The reusability of Pt/HZSM-5-F-50 in term of PHP selectivity was investigated in the deep hydrogenation of PHE. After each reaction, the spent catalyst is centrifuged and washed using cyclohexane and ethanol (repeated three times) and dried under vacuum at 80 °C, and subsequently used for the next reaction. In the reusability experiments, multiple parallel experiments were conducted to ensure that the amounts of catalyst were equal for each experiment. As shown in Fig. 5, the selectivity of PHP remained consistently above 85.0% after four catalytic cycles, indicating the good recyclability. The XRD and TGA measurements show that Pt/HZSM-5-F-50-spent still retained its original structure (Fig. S16), and no significant coke deposition was detected for Pt/HZSM-5-F-50-spent after four cycles (Fig. S17). Additionally, the dispersion and electronic states of the supported Pt species on Pt/HZSM-5-F-50-spent were not significantly changed in comparison with Pt/HZSM-5-F-50-fresh, as evidenced by the results of TEM (Fig. 2(c) and Fig. S18) and XPS (Fig. S19).

The effects of Pt loading and H_2 pressure on hydrogenation performance of PHE were investigated over Pt/HZSM-5-F-50, and the results are shown in Figs. S20–S21. As the Pt loadings increased from 0.5 to 1.0 wt%, the conversion of PHE was maintained at nearly 100%, while the PHP selectivity increased from 38.2% to 99.2% (Fig. S20). The effects of H_2 pressure on the PHE hydrogenation reaction are shown in Fig. S21. At 2.5 MPa H_2, the deep hydrogenation products sym-OHP (30.5%) and PHP (58.0%) were detected. Upon increasing the H_2 pressure to 3.0 MPa, the deep hydrogenation capability was significantly enhanced as evidenced by the higher selectivity of PHP (99.2%). However, further increase in H_2 pressure (3.5 MPa) resulted in a decrease in the selectivity of PHP, which may be due to the simultaneous isomerization of sym-OHP to asym-OHP during the hydrogenation of sym-OHP to PHP (Liu et al., 2021; Chen et al., 2022). The conversion of PHE and product selectivity over Pt/HZSM-5-F-50 were investigated as a function of reaction time over at 250 °C. As shown in Fig. S22, Pt/HZSM-5-F-50 achieved 97.0% conversion of PHE at a reaction time of 1 h and the main products obtained were DHP, sym-OHP and asym-OHP. As the reaction time increased from 2 to 10 h, the selectivity of PHP showed a gradual increase, and reached 99.2% at 10 h.

4. Conclusions

In conclusion, two series of mesoporous ZSM-5 samples with the differences in Al_F distribution but similar Si/Al ratios, that is ZSM-5-F-*x* and ZSM-5-E-*x*, were fabricated in the crystallization system with or without NaOH. The results indicate that the Al_F distribution in HZSM-5 can be tailored with or without NaOH, acidity variations arising from the differences in Al_F distribution has a pronounced effect on PHE hydrogenation performance of Pt/

HZSM-5. Various characterizations and the controlled reactions results demonstrate that the higher enrichment degree of Al_F on the external surface and the suitable arrangement mode of Al_F in ten-membered ring (10-MR) of HZSM-5-F-*x* compared to HZSM-5-E-*x* in case of the similar Si/Al ratios, result in Pt/HZSM-5-F-*x* exhibiting remarkably-improved deep hydrogenation performance for PHE compared to Pt/HZSM-5-E-*x*. In addition, the deep hydrogenation of PHE over Pt/HZSM-5 is predominantly driven by the strong acid-induced spillover hydrogenation. In particularly, Pt/HZSM-5-F-50 exhibits well deep hydrogenation performance at low temperatures (220 °C), along with good reusability. This work contributes to the comprehensive understanding of the impact of Al_F distribution in HZSM-5 on the deep hydrogenation of PAHs, potentially guiding the design and development of subsequent efficient zeolite-based catalysts for deep hydrogenation of PAHs.

CRediT authorship contribution statement

Chuan-Hao Zhang: Writing – original draft, Software, Investigation, Formal analysis, Data curation. **Qi Dong:** Software, Investigation. **Fei Wang:** Software, Investigation, Conceptualization. **Ning-Yue Lu:** Resources, Investigation. **Feng Yu:** Investigation, Formal analysis. **Bin-Bin Fan:** Writing – review & editing, Methodology, Investigation, Formal analysis, Data curation, Conceptualization. **Rui-Feng Li:** Supervision, Resources.

Declaration of competing interest

The authors declare that they have no known competing financial interests or personal relationships that could have appeared to influence the work reported in this paper.

Acknowledgments

This work was supported by the National Science Foundation of China (No.22378293) and Fundamental Research Program of Shanxi Province (No. 20210302123398).

Supplementary data

Supplementary data to this article can be found online at https://doi.org/10.1016/j.petsci.2025.09.017.

References

Beltramone, A.R., Resasco, D.E., Alvarez, W.E., et al., 2008. Simultaneous hydrogenation of multiring aromatic compounds over NiMo catalyst. Ind. Eng. Chem. Res. 47 (19), 7161–7166. https://doi.org/10.1021/ie8004258.

Chen, X., Wang, X.B., Han, S.H., et al., 2022. Overcoming limitations in the strong interaction between Pt and irreducible SiO_2 enables efficient and selective hydrogenation of anthracene. ACS Appl. Mater. 14 (1), 590–602. https://doi.org/10.1021/acsami.1c16965.

Cychosz, K., Guillet-Nicolas, R., García-Martínez, J., et al., 2017. Recent advances in the textural characterization of hierarchically structured nanoporous materials. Chem. Soc. Rev. 46 (2), 389–414. https://doi.org/10.1039/C6CS00391E.

Dang, Y., Liu, Y.B., Feng, X., et al., 2019. Effect of dispersion on the adsorption of polycyclic aromatic hydrocarbons over the γ-Al_2O_3 (110) surface. Appl. Surf. Sci. 486, 137–143. https://doi.org/10.1016/j.apsusc.2019.05.020.

Dedecek, J., Balgová, V., Pashkova, V., et al., 2012. Synthesis of ZSM-5 zeolites with defined distribution of Al atoms in the framework and multinuclear MAS NMR analysis of the control of Al distribution. Chem. Mater. 24, 3231–3239. https://doi.org/10.1021/cm301629a.

Dědeček, J., Kaucký, D., Wichterlová, B., 2000. Co^{2+} ion siting in pentasil-containing zeolites, part 3.: Co^{2+} ion sites and their occupation in ZSM-5: a VIS diffuse reflectance spectroscopy study. Microporous Mesoporous Mater. 35–36, 483–494. https://doi.org/10.1016/S1387-1811(99)00244-9.

Dědeček, J., Tabor, E., Sklenak, S., 2019. Tuning the aluminum distribution in zeolites to increase their performance in acid-catalyzed reactions. ChemSusChem. 12, 556–576. https://doi.org/10.1002/cssc.201801959.

Dědeček, J., Čapek, L., Sazama, P., et al., 2011. Control of metal ion species in zeolites by distribution of aluminium in the framework: from structural analysis to performance under real conditions of SCR-NO_x and NO, N_2O decomposition. Appl. Catal. A. 391 (1), 244–253. https://doi.org/10.1016/j.apcata.2010.06.026.

Dědeček, J., Sklenak, S., Li, C.B., et al., 2009. Effect of Al-Si-Al and Al-Si-Si-Al pairs in the ZSM-5 zeolite framework on the ^{27}Al NMR spectra. a combinedAhigh-resolution ^{27}Al NMR and DFT/MM study. J. Phys. Chem. C 113 (4), 1447–1458. https://doi.org/10.1021/jp8068333.

Derouane, E.G., Determmerie, S., Gabelica, Z., et al., 1981. Synthesis and characterization of ZSM-5 type zeolites I. Physico-chemical properties of precursors and intermediates. Appl. Catal. 1, 201–224. https://doi.org/10.1016/0166-9834(81)80007-3.

Dong, Q., Zhang, C.H., Zhang, H.F., et al., 2023. Design and preparation of Pt@SSZ-13@β core-shell catalyst for hydrocracking of naphthalene. J. Catal. 421, 365–375. https://doi.org/10.1016/j.jcat.2023.03.035.

Fu, W.Q., Zhang, L., Wu, D.F., et al., 2016. Mesoporous zeolite ZSM-5 supported Ni_2P catalysts with high activity in the hydrogenation of phenanthrene and 4,6-dimethyldibenzothiophene. Ind. Eng. Chem. Res. 55 (26), 7085–7095. https://doi.org/10.1021/acs.iecr.6b01583.

Fu, W.Q., Zhao, W.B., Zhang, L., et al., 2019. ZSM-5 microspheres consisting of nanocrystals for preparing highly dispersed MoP clusters with good activity in phenanthrene hydrogenation. Ind. Eng. Chem. Res. 58 (37), 17289–17299. https://doi.org/10.1021/acs.iecr.9b03477.

Fu, W.Q., Zhang, L., Wu, D.F., et al., 2015. Mesoporous zeolite-supported metal sulfide catalysts with high activities in the deep hydrogenation of phenanthrene. J. Catal. 330, 423–433. https://doi.org/10.1016/j.jcat.2015.07.026.

Góra-Marek, K., Tarach, K., Choi, M., 2014. 2,6-Di-tert-butylpyridine sorption approach to quantify the external acidity in hierarchical zeolites. J. Phys. Chem. C 118 (23), 12266–12274. https://doi.org/10.1021/jp501928k.

Guo, S.J., Fan, S., Wang, H., et al., 2024. Selective conversion of CO_2 to trimethylbenzene and ethene by hydrogenation over a bifunctional $ZnCrO_x$/H-ZSM-5 composite catalyst. ACS Catal. 14 (1), 271–282. https://doi.org/10.1021/acscatal.3c03689.

He, T., Wang, Y.X., Miao, P.J., et al., 2013. Hydrogenation of naphthalene over noble metal supported on mesoporous zeolite in the absence and presence of sulfur. Fuel 106, 365–371. https://doi.org/10.1016/j.fuel.2012.12.025.

Huang, L.Z., Wang, P.F., Li, J.F., et al., 2016. Effect of acid leaching and catalytic properties of zeolite [Al,B]-MWW utilized as ethene methylation catalyst. Microporous Mesoporous Mater. 223, 230–240. https://doi.org/10.1016/j.micromeso.2015.11.016.

Jia, T.H., Zhang, X.W., Liu, Y., et al., 2021. A comprehensive review of the thermal oxidation stability of jet fuels. Chem. Eng. Sci. 229, 116157. https://doi.org/10.1016/j.ces.2020.116157.

Jongpatiwut, S., Li, Z.R., Resasco, D.E., et al., 2004. Competitive hydrogenation of poly-aromatic hydrocarbons on sulfur-resistant bimetallic Pt-Pd catalysts. Appl. Catal. A. 262 (2), 241–253. https://doi.org/10.1016/j.apcata.2003.11.032.

Kubička, D., Kumar, N., Venäläinen, T., et al., 2006. Metal-support interactions in zeolite-supported noble metals: influence of metal crystallites on the support acidity. J. Phys. Chem. B. 110 (10), 4937–4946. https://doi.org/10.1021/jp055754k.

Laredo, G.C., Vega Merino, P.M., Hernández, P.S., 2018. Light cycle oil upgrading to high quality fuels and petrochemicals: a review. Ind. Eng. Chem. Res. 57 (22), 7315–7321. https://doi.org/10.1021/acs.iecr.8b00248.

Li, M.R., Huang, Y., Ju, C., et al., 2017. Release of full catalytic capacity of desilicated ZSM-5 in MTH reaction: al migration along mesopore introduction and post engineering. Microporous Mesoporous Mater. 244, 7–14. https://doi.org/10.1016/j.micromeso.2017.02.046.

Liang, T., Chen, J.L., Qin, Z.F., et al., 2016. Conversion of methanol to olefins over H-ZSM-5 zeolite: reaction pathway is related to the framework aluminum siting. ACS Catal. 6 (11), 7311–7325. https://doi.org/10.1021/acscatal.6b01771.

Lin, S.D., Vannice, M.A., 1993. Hydrogenation of aromatic hydrocarbons over supported Pt catalysts .I. benzene hydrogenation. J. Catal. 143 (2), 539–553. https://doi.org/10.1006/jcat.1993.1297.

Liu, C., Su, J.J., Liu, Su, et al., 2020a. Insights into the key factor of zeolite morphology on the selective conversion of syngas to light aromatics over a Cr_2O_3/ZSM-5 catalyst. ACS Catal. 10 (24), 15227–15237. https://doi.org/10.1021/acscatal.0c03658.

Liu, D.C., Chen, Y., Jing, J.Y., et al., 2021. Synthesis of Ni/$NiAlO_x$ catalysts for hydrogenation saturation of Phenanthrene. Front. Chem. 9. https://doi.org/10.3389/fchem.2021.757908.

Liu, J.J., Zhang, H.F., Lu, N.Y., et al., 2020b. Influence of acidity of mesoporous ZSM-5-supported Pt on naphthalene hydrogenation. Ind. Eng. Chem. Res. 59 (3), 1056–1064. https://doi.org/10.1021/acs.iecr.9b04411.

Liu, L.C., Corma, A., 2018. Metal catalysts for heterogeneous catalysis: from single atoms to nanoclusters and nanoparticles. Chem. Rev. 118 (10), 4981–5079. https://doi.org/10.1021/acs.chemrev.7b00776.

Liu, Z.Q., Wei, X.Y., Liu, F.J., et al., 2018. Temperature-controlled hydrogenation of anthracene over nickel nanoparticles supported on attapulgite powder. Fuel 223, 222–229. https://doi.org/10.1016/j.fuel.2018.03.014.

Lu, N.Y., Zhao, J.X., Dong, Q., et al., 2021a. Supported noble metal catalyst with a core-shell structure for enhancing hydrogenation performance. Mol. Catal. 506, 111543. https://doi.org/10.1016/j.mcat.2021.111543.

Lu, N.Y., Wang, H.Y., Wang, Y., et al., 2021b. Metal nanoparticles encapsulated within SOD zeolite coupling with HZSM-5 for hydrogenative conversion of methylcyclopentane. Fuel 291, 120159. https://doi.org/10.1016/j.fuel.2021.120159.

Luo, W.Q., Shi, H., Schachtl, E., et al., 2018. Active sites on nickel-promoted transition-metal sulfides that catalyze hydrogenation of aromatic compounds. Angew. Chem. Int. Ed. 57 (44), 14555–14559. https://doi.org/10.1002/anie.201808428.

Ma, Z.X., Wang, X.X., Ma, X.L., et al., 2023. Catalytic roles of acid property in different morphologies of H-ZSM-5 zeolites for syngas-to-aromatics conversion over ZnCrOx/H-ZSM-5 catalysts. Microporous Mesoporous Mater. 349, 112420. https://doi.org/10.1016/j.micromeso.2022.112420.

Mensah, J., Yan, P.H., Kennedy, E., et al., 2021. Novel hierarchical core-shell BEA@NanoZSM-5 zeolite for improved cracking performance for 1,3,5-triisopropylbenzene and *n*-hexadecane. Microporous Mesoporous Mater. 328, 111399. https://doi.org/10.1016/j.micromeso.2021.111399.

Miller, J.T., Meyers, B.L., Modica, F.S., et al., 1993. Hydrogen temperature-programmed desorption (H_2-TPD) of supported platinum catalysts. J. Catal. 143 (2), 395–408. https://doi.org/10.1006/jcat.1993.1285.

Niu, X.P., Zhao, R., Han, Y.X., et al., 2022. Highly dispersed platinum clusters anchored on hollow ZSM-5 zeolite for deep hydrogenation of polycyclic aromatic hydrocarbons. Fuel 326, 125021. https://doi.org/10.1016/j.fuel.2022.125021.

Pan, M., Liu, T.Y., Pang, Y.H., et al., 2024. High-silica hierarchical ZSM-5 prepared by conventional alkali treatment: a highly stable MTP catalyst. Fuel 365, 131245. https://doi.org/10.1016/j.fuel.2024.131245.

Peng, C., Zhou, Z.M., Cheng, Z.M., et al., 2019. Upgrading of light cycle oil to high-octane gasoline through selective hydrocracking over non-noble metal bifunctional catalysts. Energy Fuels 33 (2), 1090–1097. https://doi.org/10.1021/acs.energyfuels.8b04229.

Peng, P., Zhuang, S., Xiang, Y., et al., 2018. Combined alkali dissolution and re-assembly approach toward ZSM-5 mesostructures with extended lifetime in cumene cracking. J. Colloid Interface Sci. 529, 283–293. https://doi.org/10.1016/j.jcis.2018.06.013.

Pinilla, J.L., García, A.B., Philippot, K., et al., 2014. Carbon-supported Pd nanoparticles as catalysts for anthracene hydrogenation. Fuel 116, 729–735. https://doi.org/10.1016/j.fuel.2013.08.067.

Prins, R., 2012. Hydrogenspillover. facts and fiction. Chem. Rev. 112 (5), 2714–2738. https://doi.org/10.1021/cr200346z.

Qi, S.C., Zhang, L., Wei, X.Y., et al., 2014. Deep hydrogenation of coal tar over a Ni/ZSM-5 catalyst. RSC Adv. 4 (33), 17105–17109. https://doi.org/10.1039/C3RA47701K.

Song, S.F., Wu, Y.J., Ge, S.S., et al., 2019. A facile way to improve Pt atom efficiency for CO oxidation at low temperature: modification by transition metal oxides. ACS Catal. 9 (7), 6177–6187. https://doi.org/10.1021/acscatal.9b01679.

Tang, T.D., Yin, C.Y., Wang, L.F., et al., 2008. Good sulfur tolerance of a mesoporous beta zeolite-supported palladium catalyst in the deep hydrogenation of aromatics. J. Catal. 257 (1), 125–133. https://doi.org/10.1016/j.jcat.2008.04.013.

Thompson, R.W., 1992. Comments on the autocatalytic nucleation of (Na, TPA)-ZSM-5. Zeolites 12, 837–840. https://doi.org/10.1016/0144-2449(92)90058-W.

Wang, L., Chen, Y.J., Jin, S.H., et al., 2016. Selective ring-shift isomerization in hydroconversion of fluorene over supported platinum catalysts. Energy Fuels 30 (4), 3403–3412. https://doi.org/10.1021/acs.energyfuels.6b00360.

Wang, M.L., Qian, X.Q., Xie, L.Q., et al., 2019. Synthesis of a Ni phyllosilicate with controlled morphology for deep hydrogenation of polycyclic aromatic hydrocarbons. ACS Sustainable Chem. Eng. 7 (2), 1989–1997. https://doi.org/10.1021/acssuschemeng.8b04256.

Wang, S., Wang, P.F., Qin, Z.F., et al., 2018. Relation of catalytic performance to the aluminum siting of acidic zeolites in the conversion of methanol to olefins, viewed via a comparison between ZSM-5 and ZSM-11. ACS Catal. 8, 5485–5505. https://doi.org/10.1021/acscatal.8b01054.

Wang, X.X., Wang, C., Chu, Y.Y., et al., 2024. Deciphering the link between zeolite crystal size, Brønsted acid site distribution, and dual-cycle selectivity in methanol-to-olefins over zeolite. ACS Catal. 14, 15609–15621. https://doi.org/10.1021/acscatal.4c05555.

Yang, L.Z., Liu, Z.Y., Liu, Z., et al., 2017. Correlation between H-ZSM-5 crystal size and catalytic performance in the methanol-to-aromatics reaction. Chin. J. Catal. 38, 683–690. https://doi.org/10.1016/S1872-2067(17)62791-8.

Yokoi, T., Mochizuki, H., Namba, S., et al., 2015. Control of the Al distribution in the framework of ZSM-5 zeolite and its evaluation by solid-state NMR technique and catalytic properties. J. Phys. Chem. C. 119 (27), 15303–15315. https://doi.org/10.1021/acs.jpcc.5b03289.

Yuan, K., Jia, X.Y., Wang, S., et al., 2022. Regulating the distribution of acid sites in ZSM-11 zeolite with different halogen anions to enhance its catalytic performance in the conversion of methanol to olefins. Microporous Mesoporous Mater. 341, 112051. https://doi.org/10.1016/j.micromeso.2022.112051.

Zhang, L.W., Zhang, H.K., Chen, Z.Q., et al., 2019a. Effect of framework Al siting on catalytic performance in methanol to aromatics over ZSM-5 zeolites. J. Fuel Chem. Technol. 47 (12), 1468–1475. https://doi.org/10.1016/S1872-5813(19)30058-1.

Zhang, X.S., Lei, H.W., Zhu, L., et al., 2016. Enhancement of jet fuel range alkanes from co-feeding of lignocellulosic biomass with plastics via tandem catalytic conversions. Appl. Energy 173, 418–430. https://doi.org/10.1016/j.apenergy.2016.04.071.

Zhang, Y.T., Zhang, N.N., Chen, S.L., et al., 2022. Surface dealuminated beta zeolites supported WO_3 catalyst and its catalytic performance in tetralin hydrocracking. Pet. Sci. 19 (6), 3116–3123. https://doi.org/10.1016/j.petsci.2022.10.015.

Zhang, Y.Y., Duan, D.L., Lei, H.W., et al., 2019b. Jet fuel production from waste plastics via catalytic pyrolysis with activated carbons. Appl. Energy 251, 113337. https://doi.org/10.1016/j.apenergy.2019.113337.

Zhao, S.F., Collins, D., Wang, L.Z., et al., 2021. Influence of ZSM-5 porosity and binder introduction on the coke formation in the cracking of 1,3,5-triisopropylbenzene. Catal. Today 368, 211–216. https://doi.org/10.1016/j.cattod.2020.10.044.

Zhu, L.H., Shan, S.Y., Petkov, V., et al., 2017. Ruthenium-nickel-nickel hydroxide nanoparticles for room temperature catalytic hydrogenation. J. Mater. Chem. A. 5 (17), 7869–7875. https://doi.org/10.1039/C7TA01437F.